Ion-exchanged glass microrods as hybrid SERS/fluorescence substrates for molecular beacon-based DNA detection

Simone Berneschi[a§], Cristiano D'Andrea[a§], Francesco Baldini[a], Martina Banchelli[a], Marella De Angelis[a], Stefano Pelli[a], Roberto Pini[a], Diego Pugliese[b], Nadia G. Boetti[c], Davide Janner[b], Daniel Milanese[d], Ambra Giannetti[a*], Paolo Matteini[a]

[a] *Institute of Applied Physics "Nello Carrara", IFAC - CNR, Via Madonna del Piano 10, 50019 Sesto Fiorentino (FI), Italy*

[b] *Department of Applied Science and Technology and RU INSTM, Politecnico di Torino, Corso Duca degli Abruzzi 24, 10129 Torino, Italy*

[c] *Fondazione LINKS-Leading Innovation and Knowledge for Society, via P. C. Boggio 61, 10138 Torino, Italy*

[d] *Department of Engineering and Architecture and RU INSTM, Università di Parma, Parco Area delle Scienze 181/A, 43124 Parma, Italy*

§ *S. Berneschi and C. D'Andrea contributed equally to this work*

* *Corresponding author: a.giannetti@ifac.cnr.it*

ABSTRACT

Ion-exchange in molten nitrate salts containing metal ions (i.e.: silver, copper, etc.) represents a well-established technique able to modify the chemical-physical properties of glass materials. It is widely used not only in the field of integrated optics (IO) but, more recently, in plasmonics due to the possibility to induce the formation of metal nanoparticles in the glass matrix by an *ad hoc* thermal post-process. In this work, the application of this technology for the realization of low-cost and stable surface enhanced Raman scattering (SERS) active substrates, based on soda-lime glass microrods, is reported. The microrods, with a radius of a few tens of microns, were obtained by cutting the end of an ion-exchanged soda-lime fibre for a length less than 1 cm. As ion source, silver nitrate was selected due to the outstanding SERS properties of silver. The ion-exchange and thermal annealing post-process parameters were tuned to expose the embedded silver nanoparticles on the surface of the glass microrods, avoiding the use of any further chemical etching step. In order

to test the combined SERS/fluorescence response of these substrates, labelled molecular beacons (MBs) were immobilized on their surface for deoxyribonucleic acid (DNA) detection. Our experiments confirm that target DNA is attached on the silver nanoparticles and its presence is revealed both by SERS and fluorescence measurements. These results pave the way towards the development of low-cost and stable hybrid fibres, in which SERS and fluorescence interrogation techniques are combined in the same optical device.

Keywords: ion-exchange, silver nanoparticles, fluorescence, surface-enhanced Raman scattering, biosensor, molecular beacon

1. Introduction

Raman spectroscopy represents a powerful, non-destructive and label-free optical technique able to provide information on molecular vibrations (i.e.: the so-called molecular "fingerprint") by exploiting the inelastic scattered light from a sample under visible or near-infrared laser irradiation. This unique feature allowed for identification and detection of structural changes in molecules, cellular and tissue systems, opening up extraordinary perspectives towards the development of optical sensors for chemical/biochemical applications [1–7]. Despite these unique features, Raman technologies suffer from depending on a weak effect, Raman scattered light being a small fraction of the scattered radiation (approximately 1 in 10 million). In order to overcome this problem, one of the most effective solutions involves the excitation of localized surface plasmon resonances (LSPRs) of metal nanoparticles resulting in an increased Raman signal by several orders of magnitude and typically in the 10^4 to 10^7 range [8, 9]. This effect is at the basis of surface-enhanced Raman scattering (SERS) spectroscopy, which is able to combine ultra-sensitive detection limits with the detailed structural information content of Raman spectroscopy, and has been exploited for the development of different biomolecular detection assays and optical biosensors [10–17]. In this context, the realization of plasmonic substrates based on low-cost and simple fabrication methods and ensuring high signal enhancement and reproducibility becomes an indispensable prerequisite to be achieved [18–21].

Colloidal suspensions of metal nanoparticles, obtained either by chemical or physical methods, represent the simplest SERS substrate and they are still widely used thanks to their significant SERS performance, good stability and ease of fabrication. Nevertheless, this approach lacks reproducibility due to a difficult control in the formation of regular SERS hot-spots, especially upon the analyte addition [22, 23]. This drawback can be countered by directly immobilizing the metal nanoparticles on the surface of a planar solid sample. Strategies based on lithographic techniques, such as electron beam lithography (EBL), nanoimprinting lithography (NIL) or nanosphere lithography (NSL) to mention a few, allow a high-resolution patterning assuring improved sample

uniformity and signal reproducibility. Moreover, the use of these fabrication processes permit regular hot-spots to be generated with impressive enhancement of the SERS signal. However, they generally suffer from time-consuming and high manufacturing costs, requiring advanced machinery for their implementation (i.e.: this is especially true for EBL technique, which also presents low fabrication throughput) [24–26].

Conversely, wet chemistry-based approaches allow the rapid realisation of low-cost SERS substrates by simple functionalization of the sample surface with amino or thiol groups or by silanization followed by its immersion in a metal nanoparticle suspension to bind them on the sample surface by a self-assembling procedure. Despite a certain flexibility and repeatability, these substrates usually suffer from poor surface adhesion of the nanoparticles, which makes them unstable against any external event and consequently limiting their use as affordable SERS substrates [27, 28].

In order to overcome these limitations, glass materials with metal nanoparticles embedded into the amorphous matrix by ion-exchange technique may represent an effective route towards the realization of stable and low-cost SERS substrates [29, 30]. Indeed, due to the presence of a concentration gradient at the interface between the specimen and the ion source, this process allows to easily replace the alkaline ions (e.g. sodium, Na^+) originally present inside the glass with the metal ones (e.g. silver, Ag^+) contained in the molten salt bath in which the sample is immersed at a certain temperature [31]. A further thermal post-process, carried out in air at a temperature close to the glass transition temperature or performed by laser irradiation, induces the formation of metallic nanoparticles (NPs) inside the ion-exchanged glass matrix [32–34]. The high long-term stability of Ag NPs in ion-exchanged substrates lies in the fact that they are generally located slightly below the glass surface, typically tens/hundreds of nanometres in depth [35–37]. This preserves them from any possible silver sulfidation or oxidation phenomenon. However, in order to make them available for SERS measurements, they need to be exposed by hydrofluoric acid etching or by a thermal

annealing post-process in hydrogen atmosphere, both of which require special precautions for the safety of the operator [35, 38].

In this paper, glass microrod-based SERS active substrates are presented. Metallic silver nanoparticles were produced on the surface of these systems by means of an *ad hoc* ion-exchange technique with a subsequent thermal annealing post-process without the need of an additional chemical etching step. Moreover, rather than using simple small model molecules (such as rhodamine6G) in order to test the SERS properties of the substrates thus created, here the possibility of getting a reliable, reproducible and robust biosensing system was demonstrated by means of the use of molecular beacons (MBs), immobilized on the surface of the ion-exchanged microrods, for DNA detection [39–41]. In particular, the designed MB is specific for messenger ribonucleic acid (mRNA) for survivin, a protein highly expressed in most types of cancer. The sole MB in solution and its specificity toward mRNA for survivin, compared to not-specific targets, have already been characterised in previous reports [42–44].

Finally, the use of the MB allows to carry out measurements based on the combination of SERS and fluorescence techniques. In fact, MBs are single-stranded DNA molecules that possess a stem-loop structure, the two side-ends of which are labelled with a fluorophore and a quencher. The loop portion is designed to be complementary to the oligonucleotidic target sequence, while the stem portion is self-complementary in order to confer the so-called hairpin structure to the molecule, keeping, in absence of the target molecule, fluorophore and quencher in close proximity to each other. Since the fluorophore is characterised by an emission band that overlaps the absorption band of the quencher, this proximity causes the fluorescence of the fluorophore to be quenched by energy transfer. The hybridization of the MB with the target sequence causes the opening of the stem and then the displacement of the fluorophore from the quencher, restoring the fluorescence emission. At the same time, by anchoring the MB on the silver nanoparticles via thiol chemistry, an on/off SERS response can be obtained as a function of the distance of the fluorophore label, here working as an effective Raman tag, from the plasmonic surface. SERS experiments show the effective MB

binding on the silver nanoparticles by detecting the main spectral bands ascribed to the oligonucleotidic chain. Moreover, the capability of the anchored MB to recognise the specific target sequence is also demonstrated.

Our results pave the way towards new optical biosensing systems capable of performing multimodal measurements in order to obtain additional information on a given biological event to be monitored.

2. Materials and methods

2.1 Chemicals and reagents

All the following chemicals and reagents, tris hydrochloride (tris-HCl), magnesium chloride ($MgCl_2$) for the preparation of tris-$MgCl_2$ buffer (10 mM tris-HCl, 10 mM $MgCl_2$, pH 8), ethylenediaminetetraacetate dihydrate (EDTA) for the preparation of tris-EDTA (TE buffer) (10 mM tris-HCl, 0.1 mM EDTA, pH 8), acetone, methanol (MeOH), 4-Methylbenzenethiol, silver nitrate $AgNO_3$ (≥ 99% in purity) and sodium nitrate $NaNO_3$ (≥ 99% in purity) for ion-exchange process in glass specimens, ATTO647N-NHS-ester, were purchased from Sigma-Aldrich (Milan, Italy). The molecular beacon for survivin (labelled with both ATTO647N and Black Barry Quencher (BBQ) or with only ATTO647N) and its complementary target sequence were purchased from IBA (Göttingen, Germany).

2.2 Fabrication of SERS-active substrates in optical soda-lime glass by ion-exchange process

Commercial soda-lime glass, in the shape of uneven bulk block and bar, was made available by the Effetre Murano s.r.l. and was mechanically processed at the Fondazione LINKS and Politecnico di Torino in order to obtain polished planar samples and an optical fibre, respectively. The composition (in wt%) of the soda-lime glass was estimated by energy dispersive spectroscopy (EDS) analysis to be 70.06% SiO_2, 17.53% Na_2O, 8.87% CaO, 3.54% K_2O, with Fe_2O_3 traces at around 0.3%. Ion-exchange process was performed using a salt mixture of $NaNO_3$: $AgNO_3$ (95 : 5, mol%). Reagent grade nitrates were weighed, mixed and placed in stainless steel crucibles. The ion-

exchange temperature used for the realization of SERS-active substrates was 390 °C (± 2 °C).

2.2.1 The planar soda-lime glass waveguide (SLGW) format

The planar specimens (10 mm × 10 mm × 1.3 mm in size) were used for investigating important parameters of the ion-exchange mechanism in these glasses such as, for instance, the diffusion coefficient of silver ions in the glass and their penetration depth, which were directly obtained from the optical characterisation of the slab waveguides thus fabricated.

In a first step, a short duration of 15 min was selected for the ion-exchange process (see SLGW1 in Supplementary Information, Table S1). Before immersion in the molten salt bath, the sample was cleaned through subsequent washing steps in acetone, ethanol and distilled water (the duration of each step was about 10 min). Similarly, after ion-exchange, the specimen was washed in distilled water for 10 min in order to remove residual salt from the sample surface and make it available for optical characterisation.

In a second step, the duration of the ion-exchange process was set at 4.5 h (see SLGW2 in Supplementary Information, Table S1). The formation of silver nanoparticles was successively induced by a thermal annealing post-process performed in air at different temperatures (500 and 550 °C) and times (45 min and 3h), respectively (see planar SLGW3, SLGW4 and SLGW5 in Supplemetary Information, Table S1). Due to their larger size, the planar substrates were selected for the spectroscopic characterisation.

The information obtained from the planar substrates were the basis for the implementation of an *ad hoc* ion-exchange and thermal annealing processes for the realization of microrods starting from the soda-lime glass fibre.

2.2.2 The microrod format

The microrods were realized employing a fibre optics drawn by means of an *in-house* developed drawing tower available at the Fondazione LINKS of Torino. The tower included a furnace formed by a graphite ring that was heated by an inductor operating at 248 kHz (SAET, Torino, Italy). The

soda-lime glass bar was introduced into the furnace and drawn into fibre at a speed of 6 m/min. The diameter size of the fibre was controlled during all the drawing procedure until reaching the final value of 130 μm (± 2%). The total length of the manufactured fibre was 150 m and it was cut in several pieces, each one having a length of about 30 cm. The end of the glass fibre was then immersed in the molten salt bath for a sufficiently long time to ensure the presence of the silver ions along the overall length of the fibre diameter. The time duration for this ion-exchange process was calculated by analysing the experimental data obtained during the optical characterisation of the SLGW1 planar samples and it has been fixed at 4.5 h. After the thermal ion diffusion process, a washing step of 10 min in deionized water was used to remove the residual salt from the terminal end of the fibre. Silver nanoparticles were then grown locally in the portion of the soda-lime glass fibre previously involved in the ion-exchange, by means of a thermal annealing step performed at the same conditions (in terms of time and temperature) adopted for the corresponding planar substrate (see planar SLGW4 in Supplemetary Information, Table S1). In this way, having undergone the same fabrication process, the end of the treated glass fibre was able to give the same spectroscopic response regarding the formation of silver nanoparticles. Finally, the end of the fibre was cut to less than 1 cm in order to obtain the desired microrods. Figure 1 shows the procedure adopted for the realization of these substrates.

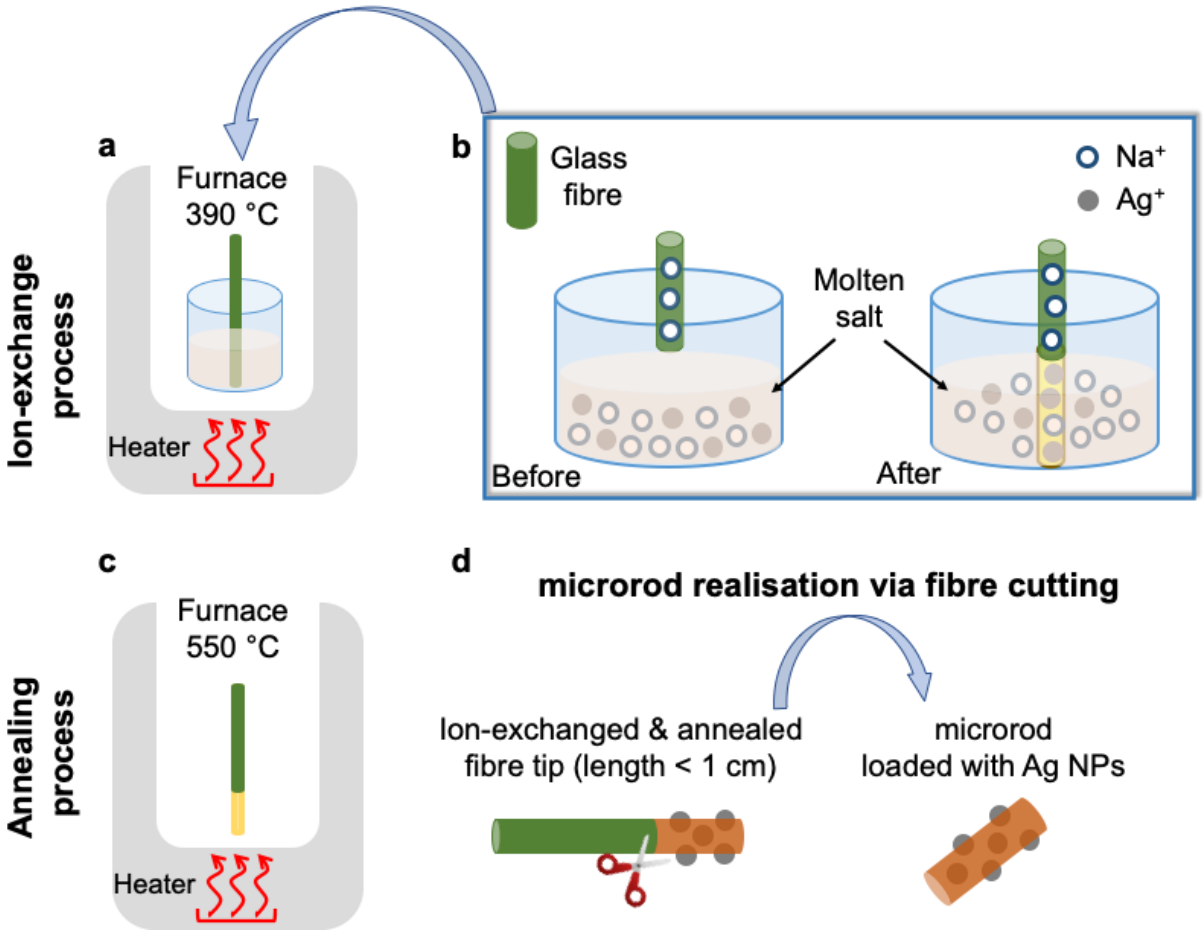

Fig. 1 (a) Sketch of the ion-exchange fabrication method for the soda-lime glass microrod; (b) the working principle of the ion-exchange process in which the sodium ions Na^+ in the glass fibre are replaced by the silver ions Ag^+ in the salt melt; (c) sketch of the thermal annealing mechanism with the formation of metallic silver nanoparticles at the end of the ion-exchanged fibre and (d) consequent microrod realisation via fibre cutting.

2.3 Optical characterisation

2.3.1 Dark-line and absorption spectroscopy of SLGW

The SLGW1 was optically characterised by means of prism-coupling technique and dark-line spectroscopy in order to measure the effective indices of the modes supported by the guiding structure so obtained [45, 46]. This was performed at the excitation wavelength of 635 nm by means of a home-made semi-automatic instrument, named COMPASSO, located at the IFAC-CNR Labs

[47]. The accuracy of the system on the effective index measurement was $\pm 1 \times 10^{-4}$. Therefore, the index profile of the waveguide in the ion-exchanged sample was calculated from the measured mode indices using the inverse Wentzel–Kramers–Brillouin (WKB) method [48, 49]. This provided an assessment of the surface index of the waveguide as well as the thickness of the exchanged layer, thus giving the value of the diffusion coefficient D_{Ag^+} of the silver ions inside the glass matrix during the ion-exchange under investigation. These data allowed us to choose the correct exchange time for the fibres.

Concerning the absorption measurements, the spectra of the planar samples were measured by a JASCO V-560 spectrophotometer, working in the range from 190 to 900 nm with a precision of 0.3 nm and operating in transmission mode.

2.3.2 SERS characterisation of microrods

Raman and SERS experiments were performed by means of a Xplora (Horiba) micro-Raman spectrometer equipped with an excitation wavelength tuned at 532 nm. The laser beam was focused through a 50× long working distance objective (Olympus, numerical aperture (NA) 0.5) on the side of microrods in a 5 µm large spot. The Raman backscattered light was collected through the same objective, analysed by a 1200 grooves/mm grating and acquired by an Andor Peltier cooled charge coupled device (CCD) detector embedded in the spectrometer. Laser power on the sample and spectral acquisition time were fixed at 110 µW and 10 s, respectively. Spectral reproducibility was confirmed acquiring different SERS maps (90 µm × 40 µm, step 10 µm) on different microrod positions. SERS activity of the ion-exchanged microrods was tested and confirmed by using 4-Methylbenzenethiol (4-MBT) as probe. The post annealed microrods were immersed for 2 h in a 10^{-4} M ethanol solution of 4-MBT before SERS detection. For comparison, a non-plasmonic Ag planar film soaked in a 10^{-2} M ethanol solution of 4-MBT for 2 h was considered.

2.3.3 Morphological characterisation by atomic force microscopy (AFM)

The morphology of the Ag-loaded soda-lime glass microrods was investigated by using AFM

technique. A JPK Nanowizard III Sense scanning probe microscopy (Bruker) working in AFM mode (maximum z-scan size 15 μm) was used. Single-beam uncoated silicon cantilever (μMash HQ:NSC15 Cr-Au BS, tip radius 7<R<10 nm) was used in tapping mode, with drive frequency between 250 and 300 kHz, and scan rate of 0.5 Hz. The acquired images were processed by using JPK SPM software, while ImageJ Particles Analyzer tool [50] was used in order to estimate the AgNPs size distribution along the microrod surface.

2.3.4 Fluorescence measurements of the DNA-hybridization-based bioassay

In order to verify the immobilisation of the MBs onto the microrods and the consequent interaction with the target sequences, fluorescence measurements of the microrods after every single step were performed using a fluorescence microscope (Zeiss AXIO Observer.Z1 inverted fluorescence microscope with a Colibri.2 light source). The microscope is equipped with a light emitting diode (LED) at 625 nm for the excitation of the ATTO647N and it was used to monitor the open and closed forms of the MB. In order to optimise the signal-to-noise ratio during the measurement acquisition, the LED source output power was kept at the maximum level and the integration time was set at 2 s.

2.4 DNA-hybridization-based bioassay for SERS and fluorescence test

Among several already published MB sequences for survivin [51–53], the selected one was chosen for its better performances in terms of folding properties and greater reactivity with the target sequence [43]. Additionally, the MB sequence was customized in order to have a modified Thymine (dT) base carrying a C_6 chain near the 3' end. The C6 chain ends with a thiol group (-SH) assuring the MB attachment to the Ag NPs. MB and target sequences are reported below:

MB: 5'-(ATTO647N)CGACGGAGAAAGGGCTGCCACGXCG(BBQ)-3' X=C6-dT Thio

Target: 5'-CCCCTGCCTGGCAGCCCTTTCTCAAGGACC-3'

Additionally, a MB sequence without BBQ was considered to be used in the assignment of the ATTO647N SERS modes.

The lyophilized MB and target sequence were resuspended in TE buffer in order to obtain several aliquots of 100 μM stock solution that were stored at -20 °C. Tests on MB reactivity once immobilized onto the ion-exchanged microrods were carried out using 1 μM final solutions of both MB and target, in tris-$MgCl_2$ buffer.

Post-annealed microrods were immersed and allowed to interact for 2 h with the MB solution and subsequently washed with tris-$MgCl_2$ buffer for the removal of non-interacted MB onto the Ag-NP of the microrod surface. Only for the case of SERS measurements, the microrods were then immersed in distilled water for removing salt residues, and finally dried in air at room temperature. After the spectroscopic characterisation, the microrods functionalized with MB were incubated for 2 h in the target sequence solutions (hereinafter, MB+T), washed and dried as previously, and the optical measurements were performed again. All the reactions and measurements were carried out at room temperature.

A scheme of the interaction between the MB and its target is represented in Fig. 2. The scheme is the same for both fluorescence and SERS configurations.

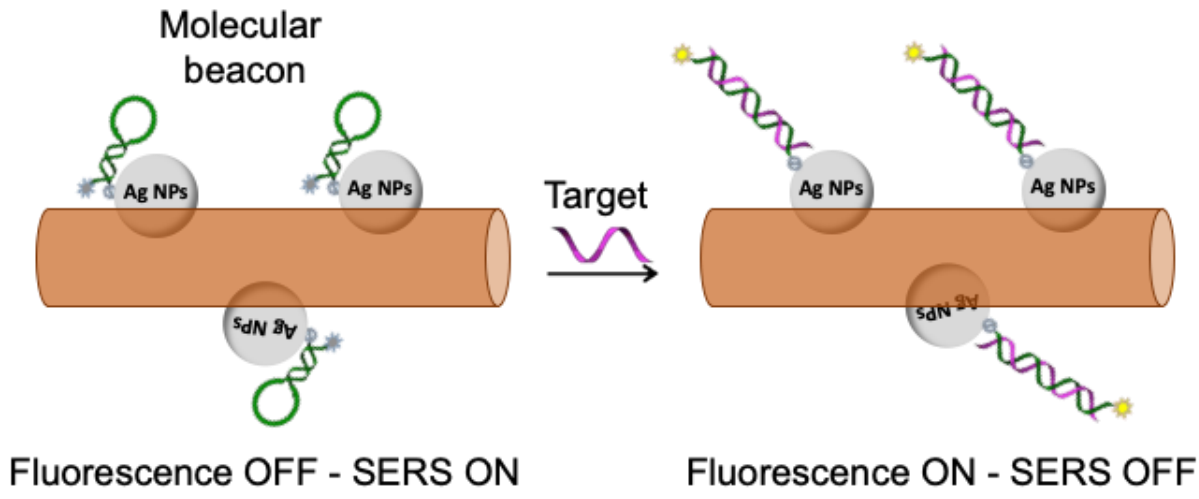

Fig. 2 Reaction scheme of the interaction between the MB and its target onto the microrod, both in fluorescence and SERS configurations.

3. Results and discussion

3.1 Optical characterisation

3.1.1 Dark-line and absorption spectroscopy of SLGW

According to optical characterisation, the SLGW1 supported 28 modes at the excitation wavelength of 635 nm. The measured effective indices ranged from 1.5128 ($\pm$ 1 $\times$ 10^{-4}) to 1.5919 ($\pm$ 1 $\times$ 10^{-4}). The value of the measured bulk refractive index (n_b) was 1.5121 ($\pm$ 2 $\times$ 10^{-4}). By applying the inverse WKB method, it was possible to reconstruct the refractive index profile as reported in Fig. 3. A Gaussian refractive index profile was selected, since it was the one which produced the best fit among the tested profiles [54]. As a result, the diffusion depth d_w, defined as the depth at which the refractive index change is 1/e of that present at the surface, was assessed to be 16 μm and the refractive index change Δn at the surface was close to 0.08.

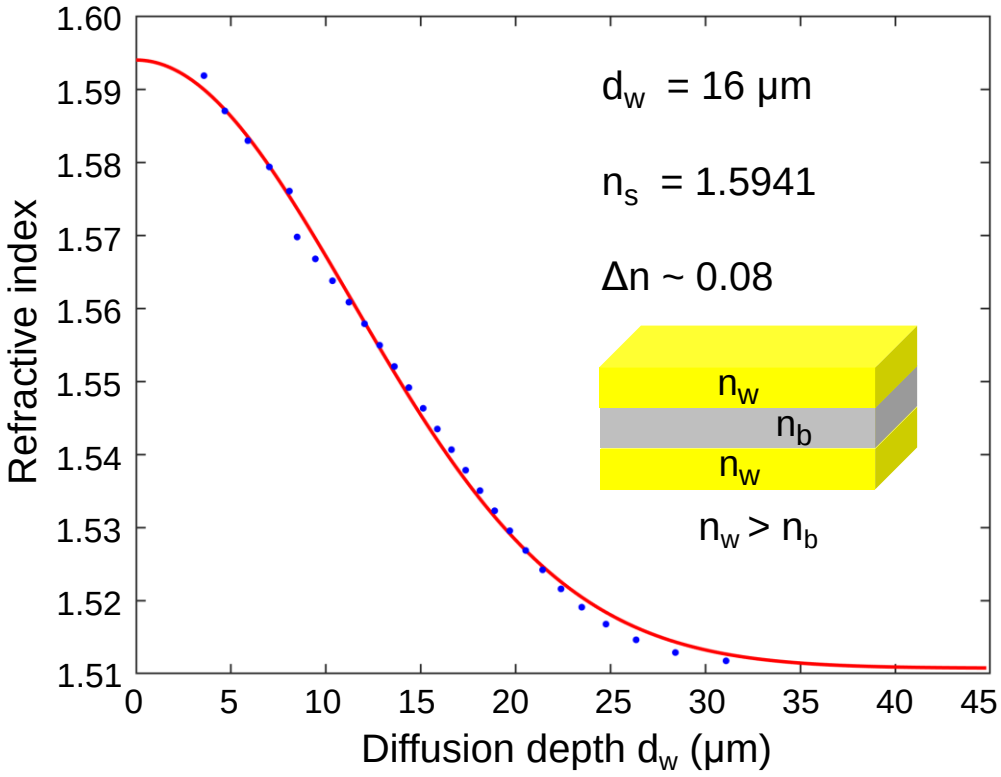

Fig. 3 The refractive index profile of the ion-exchanged SLGW1 obtained applying the inverse WKB method on the measured mode effective indices supported by the guiding structure. The blue points are the

experimental data, while the red line is the best fit obtained with Gaussian function applying the inverse WKB method. In the inset, the values of the diffusion depth of the waveguide (d_w), the surface refractive index of the waveguide (n_s), the refractive index change ($\Delta n = n_s - n_b$) and the graded refractive index profile of the waveguide (n_w) are reported.

From this analysis, the diffusion coefficient of the silver ions (D_{Ag^+}), at a given process temperature (T = 390 °C), has been assessed by inverting the formula $d_w = (D_{Ag^+} \cdot t)^{1/2}$, where t is the duration of the ion-exchange process and d_w is the diffusion depth. Moreover, the previous relationship allowed to calculate the duration of an *ad hoc* diffusive thermal process capable of loading the glass fibre with silver ions across its whole diameter. The reason behind this choice lies in the fact that, in the absence of non-exchanged regions for the glass fibre, the formation of silver nanoparticles can also be favoured at the surface of the same fibre during the subsequent thermal annealing step. In this case, the new ion-exchange time can be calculated by $t_2 = (d_f / d_w)^2 \, t_1$ where, considering the symmetry of the fibre, d_f = 65 μm, d_w = 16 μm and t_1 = 15 min. In such a way, the ion-exchange time t_2 turns out to approximately be 4.16 h. Compared to this value, a slightly longer ion-exchange time, equal to 4.5 h, was selected to further ensure the presence of silver ions throughout the entire thickness of the fibre. The new time value was thus used in the case of ion-exchange planar sample SLGW2 for the related spectroscopic characterisation.

For what concerns the absorption measurements, spectra were recorded for samples annealed at different temperature and time values (see Supplementary Information, Table S1). As shown in Fig. 4, by fixing the annealing time (t_{ann} = 45 min) and increasing the temperature, a 420 nm band gradually appeared (SLGW3 at T = 500 °C), becoming more intense and narrow at higher temperature (SLGW4 at T = 550 °C), revealing the formation of plasmonic structures. On the other hand, fixing the temperature at a certain value close to the glass transition temperature (T = 550 °C), with ever longer annealing time (from 45 min – SLGW4 – to 3 h – SLGW5) the plasmon peak intensity increased while the related band progressively broadened (Fig. 4 inset). This suggested an

increase of the silver nanoparticles size or density. For comparison, the absorbance spectrum of the bulk glass and that of the ion-exchanged specimen SLGW2 are also reported. This sample did not exhibit any absorption band around 400 nm, proving that in this specimen the ion-exchange process did not induce the formation of metallic silver nanoparticles. Only an increase in the absorbance of the ion-exchanged sample was observed in a region of the spectrum below the wavelength of 370 nm probably due to the formation of small silver clusters. All these results are in full agreement with those reported in literature [30].

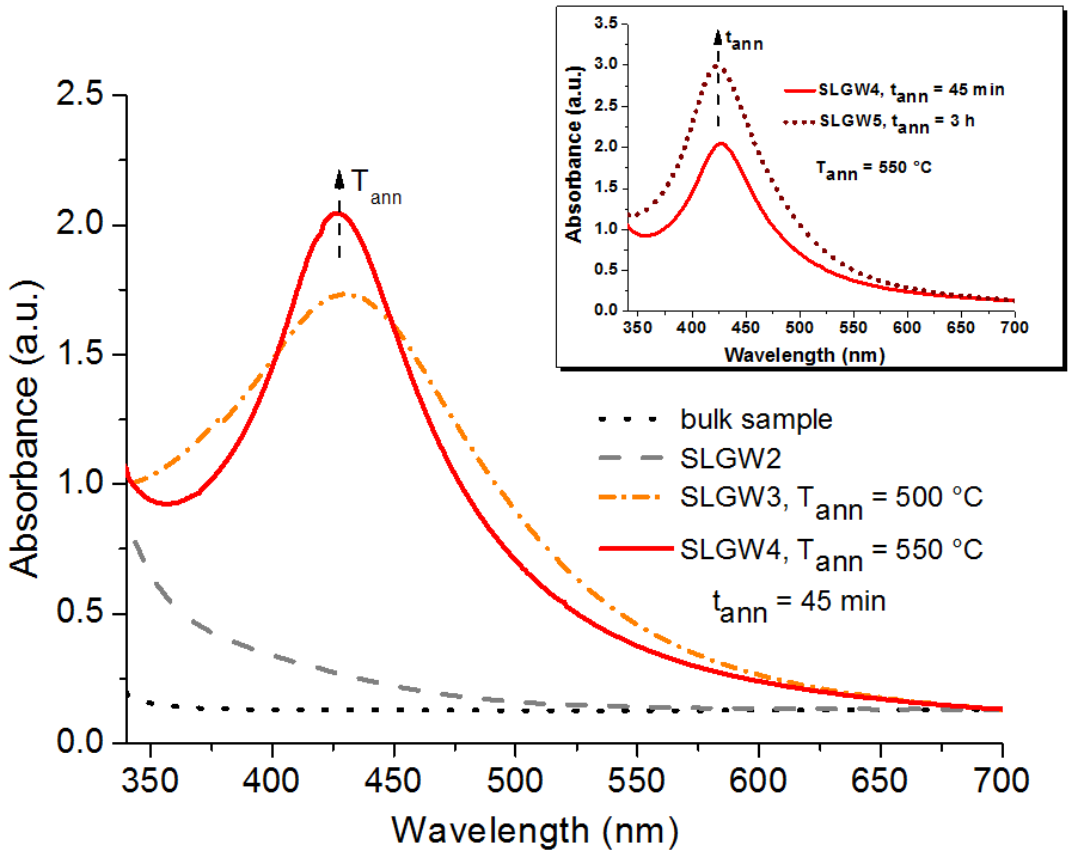

Fig. 4 Absorption spectra of the SLGW samples obtained by fixing the thermal annealing time (t_{ann} = 45 min) and changing the annealing temperature (from 500 up to 550 °C). An increase in absorbance intensity, accompanied by a narrowing of the absorption band around the wavelength of 420 nm, is clearly visible as a proof of the silver nanoparticles formation. The inset shows the absorbance peak behaviour changing the

annealing time at a fixed process temperature of 550 °C. For comparison, the absorption spectra of the bulk sample and of the not annealed ion-exchanged SLGW2 sample are also reported.

3.1.2 Morphological characterisation of ion-exchanged microrods by AFM

Heights and widths of the silver nanoparticles produced on the soda-lime surface of the microrods were measured by AFM. Figure 5a displays the topographic reconstruction of a 2 µm × 2 µm area of the microrod lateral surface (the selected treatments of which follow the scheme of SLGW4). A dense and highly packed distribution of nanoparticles is observed, with diameters ranging from few tens of nanometers to 200 nm, and a mean value of 102.4 ± 40.4 nm, calculated by fitting the size distribution with a Gaussian profile (Fig. 5b). By focusing the scan on a smaller area (500 nm × 500 nm), the previous values were confirmed by analyzing the cross-section of topographic AFM images (Fig. 5c-d). The measured apparent widths (w_{meas}) were corrected for the tip-induced broadening in the image plane, providing the real widths (w_{real}), according to the equation:

$$w_{meas} - w_{real} = 2\,(2\,R\,h - h)^{-2}$$

where h is the measured object height and R the AFM tip radius [55].

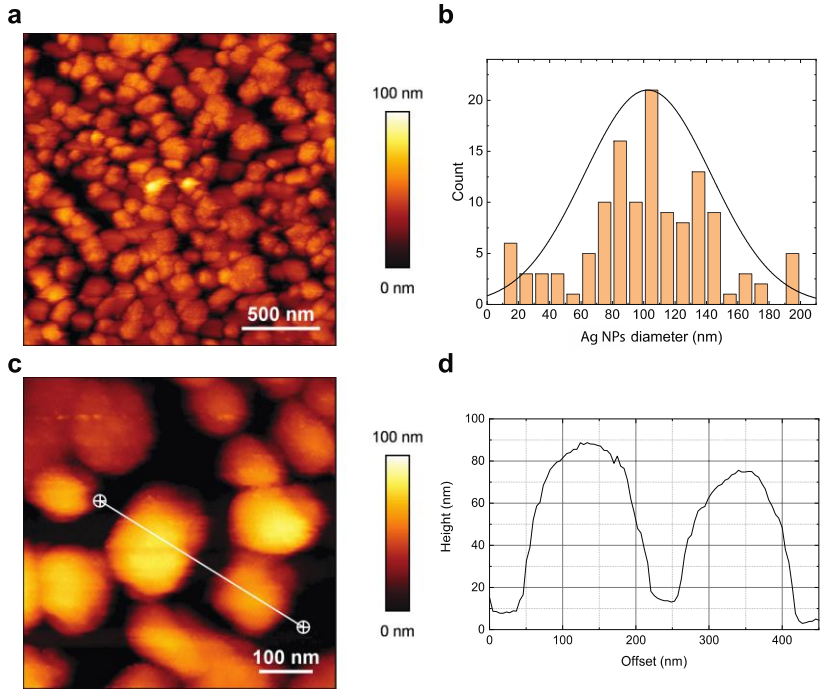

Fig. 5 Topographic AFM reconstruction of a 2 μm × 2 μm area on the side of Ag loaded microrod (the selected treatments of which follow the scheme of SLGW4) (a). The image was processed with ImageJ Particles Analyzer in order to calculate the Ag NPs diameter distribution (b), well fitted by a Gaussian curve (black line). (c) AFM image of a 500 nm × 500 nm area of microrod sample used for calculating height and diameter of Ag NPs by cross-section analysis (d).

As already mentioned, the selected procedure for this microrod preparation followed the SLGW4 steps, since this treatment offered an optimal balance between spatial and size distribution of the Ag NPs on the microrod, which was not the case of microrods as obtained at lower T_{ann} (as in SLGW3). Moreover, the SLGW4 treatment scheme offered suitable structural integrity to the microrods, which conversely declined after long annealing times (as in SLGW5).

3.1.3 Characterisation of the SERS activity

The top panel of Fig. 6 shows the comparison between the SERS spectrum of 4-MBT, obtained as the average of 50 spectra acquired from different positions of post-annealed microrod, and the spectrum obtained from an untreated microrod, immersed in the identical 4-MBT solution.

The SERS activity of the Ag nanoparticles on the surface of the ion-exchanged microrod is revealed by the presence of well-defined peaks of 4-MBT (1078, 1592 cm^{-1}) while only a fluorescence background is present in the untreated microrod. The spectrum reported in Fig. 6 was used for the calculation of the SERS gain, defined as the boost of the Raman signal due to the presence of the plasmon active NPs, by comparing the intensity of selected modes (peaked at 1078 and 1592 cm^{-1}) with the analogues acquired by a non-plasmonic Ag planar film soaked in 4-MBT solution (black curve in Fig. 6, bottom panel) [21, 55, 56]. The calculation of the SERS gain, given by the I_{SERS}/I_{Raman} ratio normalized to the 4-MBT concentration values used in SERS and Raman measurements, provides a value of 7×10^4. This value has to be considered as a lower bound estimation of the real gain since it doesn't take into account the effective SERS active surface of the hot-spots.

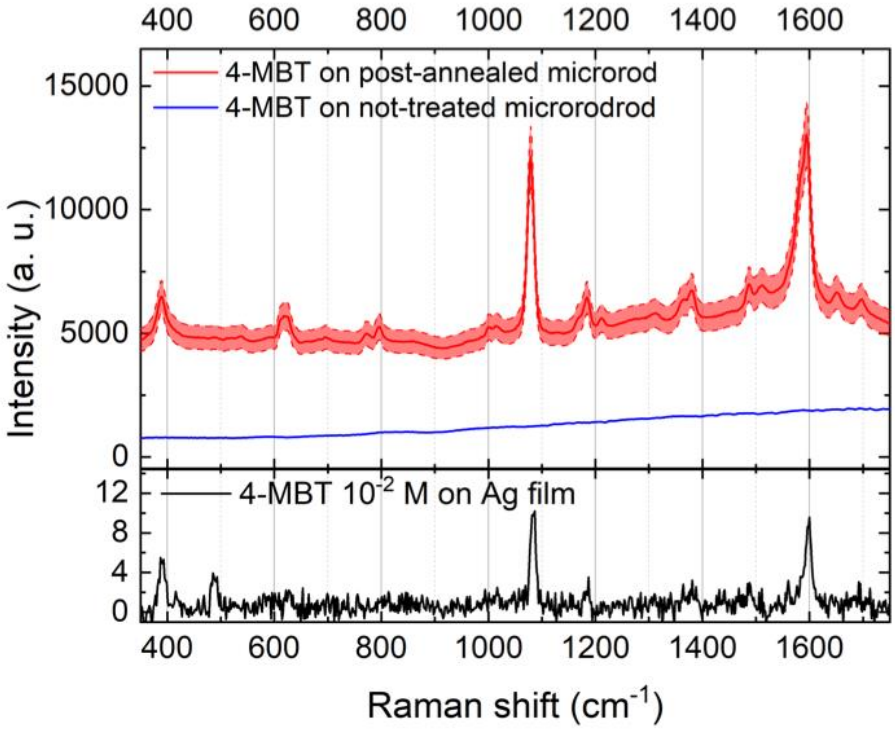

Fig. 6 SERS spectrum of 4-MBT (red line) collected on the side of a post-annealed microrod. The spectrum is the average of more than 50 spectra from different positions. Standard deviation of SERS intensities is less than 10%, and their variability is included in the area enclosed between the two dashed SERS spectra. No SERS modes of 4-MBT emerged from the analysis of an untreated microrod (blue line). Conversely, weak but characteristic Raman modes of 4-MBT can be observed from a planar non-plasmonic Ag film (black line).

3.1.4 SERS/fluorescence-based DNA-hybridization bioassay

Once demonstrated the SERS activity of the ion-exchanged microrod, a molecular beacon (MB) immobilization was carried out on the post-annealed microrod in order to test its suitability as substrate for the detection of specific oligonucleotidic sequences.

More than 100 SERS spectra were collected in random positions along the microrod surface after MB immobilization, and the average spectrum is reported in Fig. 7 (red line). SERS measurements were repeated after interaction of the MB with its specific target (hereinafter, MB+T) and their average is reported in Fig. 7 (blue line) in comparison with the spectrum of a bare post-annealed

microrod considered as background signal (black line).

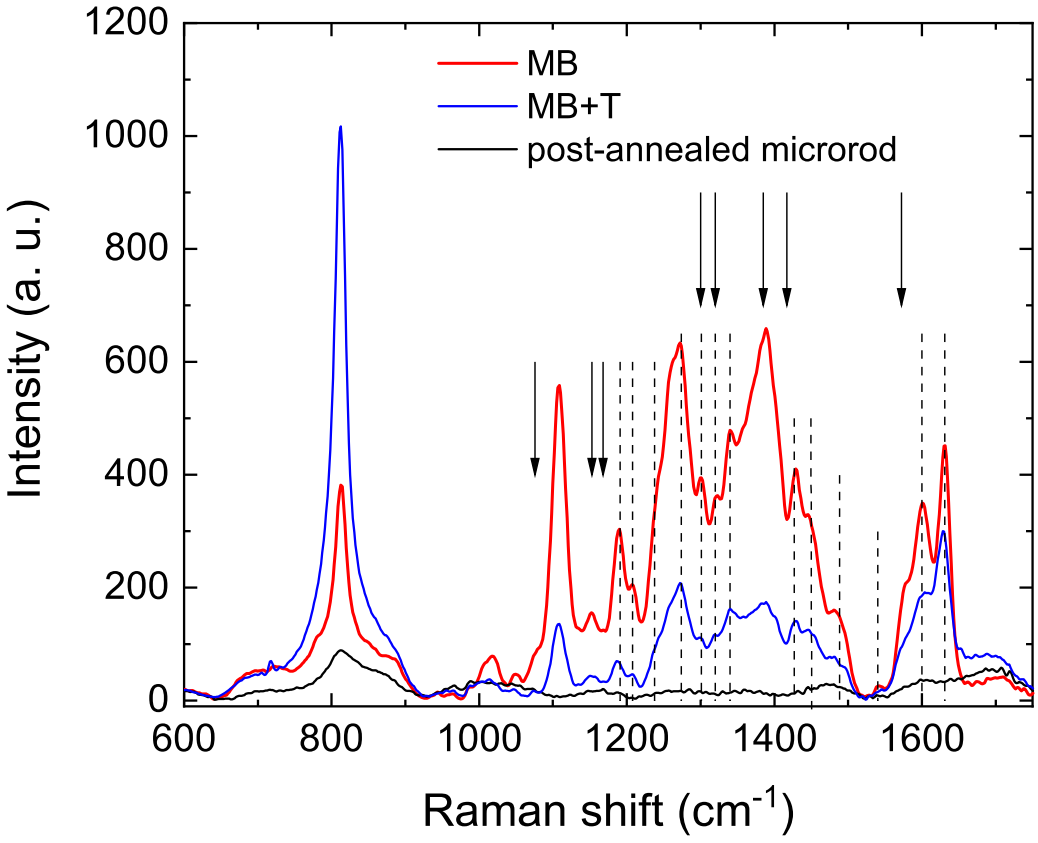

Fig.7 SERS spectra of MB on post-annealed microrod before (red line) and after the interaction with the target sequence (blue line). SERS vibrations of ATTO647N fluorophore and BBQ are highlighted by dashed lines and black arrows, respectively. The spectra are compared with the background signal from a post-annealed bare microrod (black line). All the spectra are acquired at the same experimental conditions.

According with previous literature [55, 57], spectra reported in Fig. 7 were subjected to multi-peak fitting with Lorentzian curves, in order to discriminate the SERS modes of DNA, ATTO647N and BB Quencher (see Supplementary Information, Fig. S1). The ATTO647N SERS modes were assigned after measuring the SERS profile of an MB containing the fluorophore but not the BBQ, to avoid overlapping of vibrational bands (as reported in Supplementary Information, Fig. S2). The complete assignment of the bands is summarised in Table 1.

Table 1. Tentative SERS bands assignment of MB+T

Raman shift (cm^{-1})	Tentative assignment	Ref.
812	Backbone, N-O-P-O-N sym stretch	[58]
1048	Ribose, N-sugar stretch	[59, 60]
1076	BBQ	[61]
1108		
1153	BBQ	[61]
1165	BBQ	[61]
1190	ATTO647N	this study
1210	ATTO647N	this study
1240	ATTO647N	this study
1258	A, C, ring	[58, 59, 62]
1274	ATTO647N, BBQ	this study, [61]
1301	ATTO647N, BBQ	this study, [61]
1320	ATTO647N, BBQ, A, G	this study, [59, 61]
1340	ATTO647N, BBQ	this study, [61]
1362	A, ring	[58, 60]
1381	BBQ	[61]
1417	BBQ	[61]
1427	ATTO647N	this study
1447	ATTO647N, A, G	this study, [58, 59]
1455	ATTO647N	this study
1488	ATTO647N, Ribose C_2-H_2 def	this study, [58, 59]
1541	ATTO647N	this study
1572	BBQ	[61]
1600	ATTO647N	this study
1631	ATTO647N, C (C=O stretch), BBQ	this study, [58, 59, 61, 63]

A: adenine; T: thymine; C: Cytosine; G: Guanine

The SERS modes of the ATTO647N and BBQ are highlighted in Fig. 7 by vertical dashed lines and black arrows, respectively. As expected by the complexity of the analysed sample, the SERS spectra of MB and MB+T show a dense distribution of superimposed vibrations in the 1100-1700 cm^{-1} region. Despite this complexity, a clear trend can be observed in the intensity variation of these modes when the oligonucleotide chain of the MB interacts with the target sequence. Following hybridization and subsequent elongation of the DNA chain, the increased distance between ATTO647N and the Ag NPs hot-spots on the microrod surface is induced, thus leading to an abrupt intensity decrease of the fluorophore SERS bands. On the contrary, the band peaked at 812 cm^{-1} of the double-helix backbone [64] visibly increases, confirming the MB/target interaction.

Fluorescence measurements performed on the microrods evidenced fluorescence emission changes occurring after every single step of the microrod treatment. As showed in Fig. 8, the glass itself changed its autofluorescence after ion-exchange and annealing: 123.03 ± 8.52, 179.16 ± 16.00, 74.61 ± 4.05 (not-treated microrod, ion-exchanged microrod, post-annealed microrod, respectively) as a consequence of the substitution of Na^+ by Ag^+ followed by its reduction to metal ions (Ag°). Anyhow, the autofluorescence constitutes only a low intensity background, and the fluorescence increases of almost one order of magnitude when MB is immobilised (907.23 ± 170.06), becoming even higher after the interaction of the MB with its target sequence (1906.02 ± 52.11).

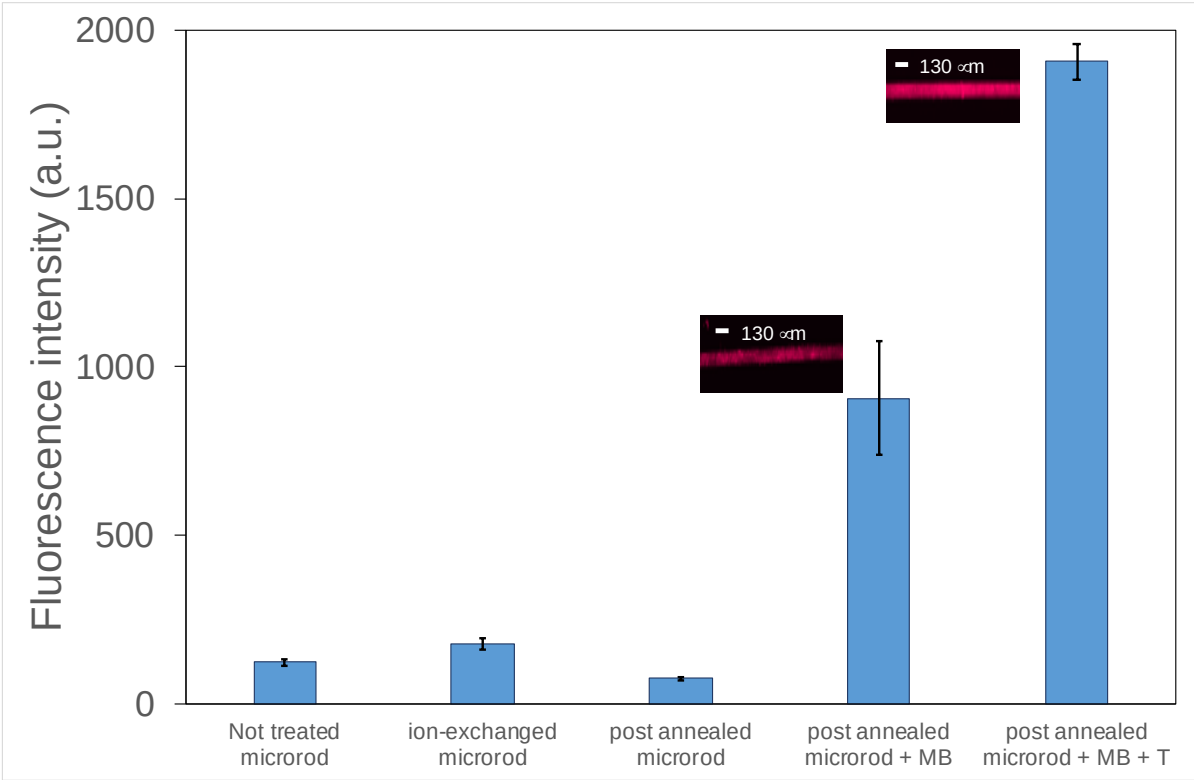

Fig. 8 The histogram shows the fluorescence intensity signal of the microrod at different treatment stages: not treated, after the ion-exchange process, after the annealing, with the MB immobilized onto the surface and after the hybridization of the MB with its specific target. In correspondence of the bars related to MB and MB + T, insets of the fluorescence images taken with the microscope are shown.

4. Conclusions and perspectives

The aim of this work was the realisation of a glass microrod-based SERS active substrate, which takes advantage of bearing stable embedded silver nanoparticles produced via ion-exchange and thermal annealing processes. In order to verify the SERS activity of the used substrate, a molecular beacon (specifically for survivin) was immobilised onto the substrate as bioreceptor for its specific oligonucleotidic target sequence. Moreover, tandem fluorescence monitoring was conducted to support SERS findings.

An ion-exchange time of 4.5 h and a furnace temperature of 390 °C were selected as preferred parameters for optimal substrate fabrication. This allowed to generate a silver ion distribution across the whole glass thickness avoiding any further necessity of chemical etching step, which requires special precautions for the safety of the operator. Afterwards, an annealing process conducted at 550 °C for 45 min triggered the reduction of silver in the form of nanoparticles. AFM measurements confirmed the presence of NPs onto the substrate surface, which were dense, highly packed distributed and with a size of 102.4 ± 40.4 nm. The performance of the SERS-active microrod was initially verified by 4-MBT detection, resulting in a SERS gain of 7×10^4. The possibility of using this kind of microrods for biosensing application was then demonstrated by immobilising a survivin-specific ATTO647N-labelled MB. SERS spectra of the MB alone compared to those collected after target addition evidenced a successful bioreceptor immobilisation and target binding according to the on/off mechanism as a consequence of the increase in the distance of the fluorophore label from the silver nanoiparticles and a concurrent increase of a double-helix backbone vibrational mode. Fluorescence measurements performed on the same microrods confirmed MB immobilisation and target interaction on the surface of the microrods according to an increase in fluorescence intensity. Therefore, unlike what has been reported in the literature so far, where the operating principle of ion exchanged-based SERS active substrates is demonstrated through the detection of a simple aromatic molecule, here their effective potential as DNA biosensors is operatively proved for the first time.

The encouraging results obtained in this work are preparatory to the development of effective hybrid optical fibres featuring an integration between a multimode silica fibre and a soft-glass microrod as a long-lasting and low-cost alternative to those realized by sophisticated and expensive lithographic processes (i.e.: EBL, NIL and NSL).

Conflicts of interests

The authors declare no conflict of interest.

Funding

C.D'A., M.B., M. de A., R.P. and P.M. acknowledge financial support from European Community and the Italian Ministry of Education University and Research within the EuroNanoMed3 ERANET cofund SPEEDY project (ID 221). D.P. and D.J. acknowledge the Interdepartmental Centre "PhotoNext" of Politecnico di Torino for the partial support of this research effort.

Acknowledgements

The authors acknowledge Effetre Murano s.r.l. for kindly providing the glass uneven bulk block and bar.

References

1. Das NK, Dai Y, Liu P, Hu C, Tong L, Chen X, Smith ZJ. Raman plus X: biomedical applications of multimodal Raman spectroscopy. Sensors. 2017;17:1592. https://doi.org/10.3390/s17071592.
2. Pence I, Mahadevan-Jansen A. Clinical instrumentation and applications of Raman spectroscopy. Chem Soc Rev. 2016;45:1958–79. https://doi.org/10.1039/c5cs00581g.
3. Schie IW, Rüger J, Mondol AS, Ramoji A, Neugebauer U, Krafft C, Popp J (2018) High-throughput screening Raman spectroscopy platform for label-free cellomics. Anal Chem. 2018;90:2023–30. https://doi.org/10.1021/acs.analchem.7b04127.
4. Li Z, Wang J, Li D. Applications of Raman spectroscopy in detection of water quality. Appl Spectrosc Rev. 2016;51:333–57. https://doi.org/10.1080/05704928.2015.1131711.
5. Germond A, Kumar V, Ichimura T, Moreau J, Furusawa C, Fujita H, Watanabe TM. Raman spectroscopy as a tool for ecology and evolution. J R Soc Interface. 2017;14:20170174. https://doi.org/10.1098/rsif.2017.0174.
6. Stokes DL, Vo-Dinh T. Development of an integrated single-fiber SERS sensor. Sens Actuators, B. 2000;69:28–36. https://doi.org/10.1016/S0925-4005(00)00291-4.
7. Barbillat J, Dhamelincourt P, Delhaye M, Da Silva E. Raman confocal microprobing, imaging and fibre- optic remote sensing: A further step in molecular analysis. J Raman Spectrosc. 1994;25:3–11. https://doi.org/10.1002/jrs.1250250103.
8. Willets KA, Van Duyne RP. Localized surface plasmon resonance spectroscopy and sensing. Annu Rev Phys Chem. 2007;58:267–97. https://doi.org/10.1146/annurev.physchem.58.032806.104607.
9. Grand J, de La Chapelle ML, Bijeon J-L, Adam P-M, Vial A, Royer P. Role of localized surface plasmons in surface-enhanced Raman scattering of shape-controlled metallic particles in regular arrays. Phys Rev B: Condens Matter Mater. 2005;72:033407. https://doi.org/10.1103/PhysRevB.72.033407.
10. Vo-Dinh T. SERS chemical sensors and biosensors: new tools for environmental and biological analysis. Sens Actuators, B. 1995;29:183–9. https://doi.org/10.1016/0925-4005(95)01681-3.
11. Ngo HT, Wang H-N, Fales AM, Vo-Dinh T. Label-free DNA biosensor based on SERS molecular sentinel on nanowave chip. Anal Chem. 2013;85:6378–83. https://doi.org/10.1021/ac400763c.
12. Wang H-N, Register JK, Fales AM, Gandra N, Cho EH, Boico A, Palmer GM, Klitzman B, Vo-Dinh T. Surface-enhanced Raman scattering nanosensors for *in vivo* detection of nucleic acid targets in a large animal model. Nano Res. 2018;11:4005–16. https://doi.org/10.1007/s12274-018-1982-3.
13. Kahraman M, Mullen ER, Korkmaz A, Wachsmann-Hogiu S. Fundamentals and applications of SERS-based bioanalytical sensing. Nanophotonics 2017;6:831–52. https://doi.org/10.1515/nanoph-2016-0174.
14. Li P, Long F, Chen W, Chen J, Chu PK, Wang H. Fundamentals and applications of surface-enhanced Raman spectroscopy–based biosensors. Curr Opin Biomed Eng. 2020;13:51–9. https://doi.org/10.1016/j.cobme.2019.08.008.
15. Banchelli M, de Angelis M, D'Andrea C, Pini R, Matteini P. Triggering molecular assembly at the mesoscale for advanced Raman detection of proteins in liquid. Sci Rep. 2018;8:1033. https://doi.org/10.1038/s41598-018-19558-w.
16. Matteini P, Cottat M, Tavanti F, Panfilova E, Scuderi M, Nicotra G, Menziani MC, Khlebtsov N, de Angelis M, Pini R. Site-selective surface-enhanced Raman detection of proteins. ACS Nano. 2017;11:918–26. https://doi.org/10.1021/acsnano.6b07523.
17. Matteini P, de Angelis M, Ulivi L, Centi S, Pini R. Concave gold nanocube assemblies as nanotraps for surface-enhanced Raman scattering-based detection of proteins. Nanoscale.

2015;7:3474–80. https://doi.org/10.1039/c4nr05704j.
18. Fan M, Andrade GFS, Brolo AG. A review on the fabrication of substrates for surface enhanced Raman spectroscopy and their applications in analytical chemistry. Anal Chim Acta. 2011;693:7–25. https://doi.org/10.1016/j.aca.2011.03.002.
19. Shiohara A, Wang Y, Liz-Marzán LM. Recent approaches toward creation of hot spots for SERS detection. J Photochem Photobiol, C. 2014;21:2–25. https://doi.org/10.1016/j.jphotochemrev.2014.09.001.
20. Mosier-Boss PA. Review of SERS substrates for chemical sensing. Nanomaterials 2017;7:142. https://doi.org/10.3390/nano7060142.
21. Banchelli M, Amicucci C, Ruggiero E, D'Andrea C, Cottat M, Ciofini D, Osticioli I, Ghini G, Siano S, Pini R, de Angelis M, Matteini P. Spot-on SERS detection of biomolecules with laser-patterned dot arrays of assembled silver nanowires. ChemNanoMat. 2019;5:1036–43. https://doi.org/10.1002/cnma.201900035.
22. Vinod M, Gopchandran KG. Au, Ag and Au:Ag colloidal nanoparticles synthesized by pulsed laser ablation as SERS substrates. Prog Nat Sci Mater Int. 2014;24:569–78. https://doi.org/10.1016/j.pnsc.2014.10.003.
23. Barbara A, Dubois F, Ibanez A, Eng LM, Quémerais P. SERS correlation spectroscopy of silver aggregates in colloidal suspension: quantitative sizing down to a single nanoparticle. J Phys Chem C. 2014;118:17922–31. https://doi.org/10.1021/jp5024444.
24. Vaiano P, Carotenuto B, Pisco M, Ricciardi A, Quero G, Consales M, Crescitelli A, Esposito E, Cusano A. Lab on Fiber Technology for biological sensing applications. Laser Photonics Rev. 2016;10:922–61. https://doi.org/10.1002/lpor.201600111.
25. Kostovski G, White DJ, Mitchell A, Austin MW, Stoddart PR. Nanoimprinted optical fibres: Biotemplated nanostructures for SERS sensing. Biosens Bioelectron. 2009;24:1531–5. https://doi.org/10.1016/j.bios.2008.10.016.
26. Quero G, Zito G, Managò S, Galeotti F, Pisco M, De Luca AC, Cusano A. Nanosphere lithography on fiber: towards engineered lab-on-fiber SERS optrodes. Sensors. 2018;18:680. https://doi.org/10.3390/s18030680.
27. Wang L, Li H, Tian J, Sun X. Monodisperse, micrometer-scale, highly crystalline, nanotextured Ag dendrites: rapid, large-scale, wet-chemical synthesis and their application as SERS substrates. ACS Appl Mater Interfaces. 2010;2:2987–91. https://doi.org/10.1021/am100968j.
28. Yuan Y, Panwar N, Yap SHK, Wu Q, Zeng S, Xu J, Tjin SC, Song J, Qu J, Yong K-T. SERS-based ultrasensitive sensing platform: An insight into design and practical applications. Coord Chem Rev. 2017;337:1–33. https://doi.org/10.1016/j.ccr.2017.02.006.
29. Simo A, Joseph V, Fenger R, Kneipp J, Rademann K. Long-term stable silver subsurface ion-exchanged glasses for SERS applications. ChemPhysChem. 2011;12:1683–8. https://doi.org/10.1002/cphc.201100098.
30. Simo A, Polte J, Pfänder N, Vainio U, Emmerling F, Rademann K. Formation mechanism of silver nanoparticles stabilized in glassy matrices. J Am Chem Soc. 2012;134:18824–33. https://doi.org/10.1021/ja309034n.
31. Tervonen A, Honkanen SK, West BR. Ion-exchanged glass waveguide technology: a review. Opt Eng. 2011;50:071107. https://doi.org/10.1117/1.3559213.
32. Karvonen L, Chen Y, Säynätjoki A, Taiviola K, Tervonen A, Honkanen S. SERS-active silver nanoparticle aggregates produced in high-iron float glass by ion exchange process. Opt Mater. 2011;34:1–5. https://doi.org/10.1016/j.optmat.2011.06.021.
33. Manzani D, Franco DF, Afonso CRM, Sant'Ana AC, Nalin M, Ribeiro SJL. A new SERS substrate based on niobium lead-pyrophosphate glasses obtained by Ag^{+}/Na^{+} ion exchange. Sens Actuators, B. 2018;277:347–52. https://doi.org/10.1016/j.snb.2018.08.113.
34. Tite T, Ollier N, Sow MC, Vocanson F, Goutaland F. Ag nanoparticles in soda-lime glass grown by continuous wave laser irradiation as an efficient SERS platform for pesticides

detection. Sens Actuators, B. 2017;242:127–31. https://doi.org/10.1016/j.snb.2016.11.006.
35. Chen Y, Karvonen L, Säynätjoki A, Ye C, Tervonen A, Honkanen S. Ag nanoparticles embedded in glass by two-step ion exchange and their SERS application. Opt Mater Express. 2011;1:164–72. https://doi.org/10.1364/ome.1.000164.
36. Babich E, Kaasik V, Redkov A, Maurer T, Lipovskii A. SERS-active pattern in silver-ion-exchanged glass drawn by infrared nanosecond laser. Nanomaterials 2020;10:1849. https://doi.org/10.3390/nano10091849.
37. Miotello A, Bonelli M, De Marchi G, Mattei G, Mazzoldi P, Sada C, Gonella F. Formation of silver nanoclusters by excimer-laser interaction in silver-exchanged soda-lime glass. Appl Phys Lett. 2011;79:2456–8. https://doi.org/10.1063/1.1406984.
38. Redkov A, Chervinskii S, Baklanov A, Reduto I, Zhurikhina V, Lipovskii A. Plasmonic molecules via glass annealing in hydrogen. Nanoscale Res Lett. 2014;9:606. https://doi.org/10.1186/1556-276X-9-606.
39. Yang CJ, Tan W. Molecular beacons. 1st ed. Berlin, Heidelberg: Springer; 2013.
40. Ratajczak K, Krazinski BE, Kowalczyk AE, Dworakowska B, Jakiela S, Stobiecka M. Optical biosensing system for the detection of survivin mRNA in colorectal cancer cells using a graphene oxide carrier-bound oligonucleotide molecular beacon. Nanomaterials 2018;8:510. https://doi.org/10.3390/nano8070510.
41. Li H, Tang Y, Zhao W, Wu Z, Wang S, Yu R. Palindromic molecular beacon-based intramolecular strand-displacement amplification strategy for ultrasensitive detection of K-ras gene. Anal Chim Acta. 2019;1065:98–106. https://doi.org/10.1016/j.aca.2019.02.059.
42. Giannetti A, Barucci A, Cosi F, Pelli S, Tombelli S, Trono C, Baldini F. Optical fiber nanotips coated with molecular beacons for DNA detection. Sensors. 2015;15:9666–80. https://doi.org/10.3390/s150509666.
43. Carpi S, Fogli S, Giannetti A, Adinolfi B, Tombelli S, Da Pozzo E, Vanni A, Martinotti E, Martini C, Breschi MC, Pellegrino M, Nieri P, Baldini F. Theranostic properties of a survivin-directed molecular beacon in human melanoma cells. PLoS One. 2014;9:e114588. https://doi.org/10.1371/journal.pone.0114588.
44. Adinolfi B, Pellegrino M, Giannetti A, Tombelli S, Trono C, Sotgiu G, Varchi G, Ballestri M, Posati T, Carpi S, Nieri P, Baldini F. Molecular beacon-decorated polymethylmethacrylate core-shell fluorescent nanoparticles for the detection of survivin mRNA in human cancer cells. Biosens Bioelectron. 2017;88:15–24. https://doi.org/10.1016/j.bios.2016.05.102.
45. Monneret S, Huguet-Chantôme P, Flory F. *m*-lines technique: prism coupling measurement and discussion of accuracy for homogeneous waveguides. J Opt A: Pure Appl Opt. 2000;2:188–95. https://doi.org/10.1088/1464-4258/2/3/304.
46. Marzuki A, Gregorius SD. Modal characterization of planar waveguide formed by Ag^+/Na^+ ion exchange in soda lime glass. IOP Conf Ser: Mater Sci Eng. 2020;858:012050. https://doi.org/10.1088/1757-899X/858/1/012050.
47. Rey-García F, Flores-Arias MT, Gómez-Reino C, De La Fuente GF, Assenmacher W, Mader W, Berneschi S, Pelli S, Nunzi-Conti G, Righini GC. Structural and optical characterization of ZrO_2:CeO_2 slab waveguides obtained via sol–gel. Opt Mater. 2012;35:97–101. https://doi.org/10.1016/j.optmat.2012.07.016.
48. Yip GL, Albert J. Characterization of planar optical waveguides by K^+-ion exchange in glass. Opt Lett. 1985;10:151–3. https://doi.org/10.1364/OL.10.000151.
49. Chiang K. Construction of refractive-index profiles of planar dielectric waveguides from the distribution of effective indexes. J Lightwave Technol. 1985;3:385–91. https://doi.org/10.1109/JLT.1985.1074194.
50. Schneider CA, Rasband WS, Eliceiri KW. NIH Image to ImageJ: 25 years of image analysis. Nat Methods. 2012;9:671–5. https://doi.org/10.1038/nmeth.2089.
51. Nitin N, Santangelo PJ, Kim G, Nie S, Bao G. Peptide-linked molecular beacons for efficient

delivery and rapid mRNA detection in living cells. Nucleic Acids Res. 2004;32:e58. https://doi.org/10.1093/nar/gnh063.
52. Santangelo PJ, Nix B, Tsourkas A, Bao G. Dual FRET molecular beacons for mRNA detection in living cells. Nucleic Acids Res. 2004;32:e57. https://doi.org/10.1093/nar/gnh062.
53. Qiao G, Gao Y, Li N, Yu Z, Zhuo L, Tang B. Simultaneous detection of intracellular tumor mRNA with bi-color imaging based on a gold nanoparticle/molecular beacon. Chem Eur J. 2011;17:11210–5. https://doi.org/10.1002/chem.201100658.
54. Zhenguang H, Srivastava R, Ramaswamy RV. Low-loss small-mode passive waveguides and near-adiabatic tapers in BK7 glass. J Lightwave Technol. 1989;7:1590–6. https://doi.org/10.1109/50.39102.
55. D'Andrea C, Foti A, Cottat M, Banchelli M, Capitini C, Barreca F, Canale C, de Angelis M, Relini A, Maragò OM, Pini R, Chiti F, Gucciardi PG, Matteini P. Nanoscale discrimination between toxic and nontoxic protein misfolded oligomers with tip-enhanced Raman spectroscopy. Small. 2018;14:1800890. https://doi.org/10.1002/smll.201800890.
56. Fazio B, D'Andrea C, Foti A, Messina E, Irrera A, Donato MG, Villari V, Micali N, Maragò OM, Gucciardi PG. SERS detection of biomolecules at physiological pH via aggregation of gold nanorods mediated by optical forces and plasmonic heating. Sci Rep. 2016;6:26952. https://doi.org/10.1038/srep26952.
57. Barucci A, D'Andrea C, Farnesi E, Banchelli M, Amicucci C, de Angelis M, Hwang B, Matteini P. Label-free SERS detection of proteins based on machine learning classification of chemo-structural determinants. Analyst. 2021;146:674–82. https://doi.org/10.1039/d0an02137g.
58. Coluccio ML, Gentile F, Das G, Perozziello G, Malara N, Alrasheed S, Candeloro P, Di Fabrizio E. From nucleotides to DNA analysis by a SERS substrate of a self similar chain of silver nanospheres. J Opt. 2015;17:114021. https://doi.org/10.1088/2040-8978/17/11/114021.
59. Peticolas WL. Raman spectroscopy of DNA and proteins. Methods Enzymol. 1995; 246:389–416. https://doi.org/10.1016/0076-6879(95)46019-5.
60. Treffer R, Lin X, Bailo E, Deckert-Gaudig T, Deckert V. Distinction of nucleobases – A tip-enhanced Raman approach. Beilstein J Nanotechnol. 2011;2:628–37. https://doi.org/10.3762/bjnano.2.66.
61. Kuzmin AN, Pliss A, Lim C-K, Heo J, Kim S, Rzhevskii A, Gu B, Yong K-T, Wen S, Prasad PN. Resonance Raman probes for organelle-specific labeling in live cells. Sci Rep. 2016;6:28483. https://doi.org/10.1038/srep28483.
62. Movileanu L, Benevides JM, Thomas GJ. Temperature dependence of the Raman spectrum of DNA. II. Raman signatures of premelting and melting transitions of poly(dA)·poly(dT) and comparison with poly(dA-dT)·poly(dA-dT). Biopolymers. 2002;63:181–94. https://doi.org/10.1002/bip.10022.
63. Guerrini L, Krpetić Ž, van Lierop D, Alvarez-Puebla RA, Graham D. Direct surface-enhanced Raman scattering analysis of DNA duplexes. Angew Chem Int Ed. 2015;54:1144–8. https://doi.org/10.1002/anie.201408558.
64. Peticolas WL, Evertsz E. Conformation of DNA *in Vitro* and *in Vivo* from laser Raman scattering. Methods Enzymol. 1992;211:335–52. https://doi.org/10.1016/0076-6879(92)11019-F.